

# Exploring the formation of spheroidal galaxies out to $z \sim 1.5$ in GOODS

Ignacio Ferreras<sup>1\*</sup>, Thorsten Lisker<sup>2</sup>, Anna Pasquali<sup>3</sup> and Sugata Kaviraj<sup>1,4</sup>

<sup>1</sup> Mullard Space Science Laboratory, University College London, Holmbury St Mary, Dorking, Surrey RH5 6NT

<sup>2</sup> Astronomisches Rechen-Institut, Zentrum für Astronomie, Universität Heidelberg, Mönchhofstr. 12-14, D-69120 Heidelberg, Germany

<sup>3</sup> Max-Planck-Institut für Astronomie, Königstuhl 17, D-69117 Heidelberg, Germany

<sup>4</sup> Astrophysics subdepartment, The Denys Wilkinson Building, Keble Road, Oxford OX1 3RH

Submitted for publication in MNRAS

## ABSTRACT

The formation of massive spheroidal galaxies is studied on a visually classified sample extracted from the ACS/*HST* images of the GOODS North and South fields, covering a total area of 360 arcmin<sup>2</sup>. The sample size (910 galaxies brighter than  $i_{F775W} = 24$ ) allows us to explore in detail the evolution over a wide range of redshifts ( $0.4 < z < 1.5$ ; median redshift 0.68). Three key observables are considered: comoving number density, internal colour distribution; and the Kormendy relation. The comoving number density of the most massive galaxies is found not to change significantly with redshift. Extrapolation of our sample to  $z=0$  gives an increase of the comoving number density of  $M_s > 10^{11} M_\odot$  galaxies by a factor 2 between  $z=1$  and  $z=0$ , in contrast with a factor  $\sim 50$  for lower mass galaxies ( $10^{10} < M_s/M_\odot < 10^{11}$ ). One quarter of the whole sample of early-types are photometrically classified as blue galaxies. On a volume-limited sample out to  $z < 0.7$ , the average stellar mass of the blue ellipticals is  $5 \cdot 10^9 M_\odot$  compared to  $4 \cdot 10^{10} M_\odot$  for red ellipticals. On a volume-limited subsample out to  $z=1.4$  probing the brightest galaxies ( $M_V < -21$ ) we find the median redshift of blue and red early-types: 1.10 and 0.85, respectively. Blue early-types only amount to 4% of this sample (compared to 26% in the full sample). The intrinsic colour distribution correlates overall bluer colours with *blue cores* (positive radial gradients of colour), suggesting an inside-out process of formation. The redshift evolution of the observed colour gradients is incompatible with a significant variation in stellar age within each galaxy. The slope of the Kormendy relation in the subsample of massive galaxies does not change over  $0.4 < z < 1.4$  and is compatible with  $z=0$  values. The “zero point” of the Kormendy Relation (i.e. the surface brightness at a fixed half-light radius) is 1 mag fainter (in the *B* band) for the subsample of low-mass ( $M_s < 3.5 \cdot 10^{10} M_\odot$ ) early-types.

**Key words:** galaxies: elliptical and lenticular, cD - galaxies: evolution - galaxies: stellar content

## 1 INTRODUCTION

For several decades the formation of luminous early-type galaxies has occupied a central debate in observational astrophysics. A comprehensive literature on these objects has convincingly established that the bulk of the star formation in these systems takes place at high redshift ( $z \gtrsim 2$  e.g. Bower et al. 1992; Stanford et al. 1998) with possibly no star formation activity thereafter – a model that is often referred to as the ‘monolithic collapse hypothesis’. This is borne out primarily by the *optical* properties of early-type populations and their strict obedience to simple scaling relations over a large range in redshift. This includes the small scatter in the early-type ‘Fundamental Plane’ (e.g. Jørgensen et al.

1996; Saglia et al. 1997) and its lack of evolution with look-back time (e.g. Forbes et al. 1998; van Dokkum & Franx 1996), the homogeneity and lack of redshift evolution in their optical colours (Bower et al. 1992; Ellis et al. 1997; Stanford et al. 1998; van Dokkum et al. 2000) and evidence for short ( $< 1$  Gyr) star formation timescales in these systems, deduced from the overabundance of  $\alpha$  elements (e.g. Thomas et al. 1999).

While the monolithic hypothesis reproduces the optical properties of early-type galaxies remarkably well, it does not sit comfortably within the currently accepted  $\Lambda$ CDM galaxy formation paradigm, in which early-type galaxies are thought to form through a hierarchical buildup process. Semi-analytical models, that combine simulations of hierarchical structure formation with simple recipes to describe the baryonic physics (star formation, chemical enrichment and feedback from the supernovae and active galactic

\* E-mail: ferreras@star.ucl.ac.uk

nuclei) have enjoyed broad success in reproducing several properties of the galaxy population in the low redshift Universe (see e.g. Cole et al. 2000; Hatton et al. 2003).

While the predicted bulk *photometric* properties of early-type galaxies have met with reasonable success (e.g. Kaviraj et al. 2005; De Lucia et al. 2006; Kaviraj et al. 2007; Kaviraj 2008), difficulties have remained in reproducing the short star formation timescales implied by the high alpha-enhancement ratios. While improved prescriptions may produce better agreement to the observed ratios (Pipino et al. 2008, in preparation) this remains one of the most important challenges to the current incarnation of semi-analytical models in terms of reproducing the properties of early-type galaxies.

Nevertheless, the discovery, using rest-frame UV data, of widespread low-level recent star formation (RSF) in early-type galaxies, both at low redshift (Kaviraj et al. 2007) and at intermediate redshifts (Ferreras & Silk 2000; Kaviraj et al. 2008), points towards a more extended star formation history than previously envisaged. While much of the work that underpins monolithic collapse was conducted in the nearby Universe, early-type populations at higher redshift are rapidly becoming available through deep optical surveys. These surveys offer an unprecedented window into the star formation histories of early-type galaxies over the last 8 billion years, crucial for understanding their formation and evolution.

Surveys that combine ground-based photometry with imaging from the WFPC2 and ACS cameras on board the *Hubble Space Telescope* (*HST*) additionally provide the angular resolution (FWHM  $\sim 0.1''$ ) to perform spatially resolved analyses of stellar populations down to physical projected sizes of  $\sim 1$  kpc at  $z \sim 1$  (e.g. Ferreras et al. 2005). In agreement with their low-redshift counterparts, recent studies that have exploited such early-type data at intermediate redshifts have found that the bulk of the star formation in these objects does indeed form at high redshift. However, tell-tale signatures of the recent star formation found in the UV studies are clearly visible. A significant fraction of early-types (up to 20%) exhibit blue cores that are characteristic of recent star formation (Menanteau et al. 2001; Ferreras et al. 2005; Pasquali et al. 2006). Furthermore, spectroscopy has revealed [OII] emission lines in a similar fraction of field early-type galaxies (Schade et al. 1999; Treu et al. 2002).

We present in this paper an extension of the sample in Ferreras et al. (2005) – which was restricted to CDFS – to the full coverage of the ACS/*HST* images of the GOODS North and South fields. However, notice that the sample presented here *does not* apply the selection based on the Kormendy relation in contrast to Ferreras et al. (2005). The only constraint applied on the sample selection is visual classification. The depth and superb angular resolution of the images enable us to accurately determine sizes and total magnitudes (which translate into stellar masses). We can determine in a robust way the *internal* colour distribution and the Kormendy relation, out to redshifts  $z \lesssim 1.2$ . We improve on Ferreras et al. (2005) by constraining the selection method to visual classification (i.e. removing the Kormendy Relation constraint) and by selecting volume-limited subsamples.

## 2 THE SAMPLE

We describe in this section the definition of our *i*-band selected (F775W), visually classified sample of early-type galaxies. The sample is extracted from the ACS/*HST* images of the Great Observatories Origins Deep Survey (GOODS; Giavalisco et al. 2004).

Both North and South fields are included, covering a total area of  $320 \text{ arcmin}^2$  equally split between the two fields. The images consist of four deep exposures through ACS passbands F435W (*B*), F606W (*V*), F775W (*i*) and F850LP (*z*). The images are drizzled with a final pixel size of 30 mas and include a weight map used for the estimates of photometric uncertainties. The weight maps also allow us to generate realistic mock galaxies used to assess the accuracy of the half-light radii (see appendix A). The visual classification was performed on the version 1.0 images, whereas all the subsequent work: photometry, size determination and intrinsic colour distribution was done on the recently released version 2.0 images (Giavalisco and the GOODS Team, in preparation). This version has a significant increase in the S/N of the *z* and the *i* bands. The methodology presented in this paper was already applied to the v1.0 images. We find an improvement on the photometric and size uncertainties, but no major difference in the overall behaviour of the sample.

### 2.1 Size and Magnitude Estimation

We started by selecting all objects with magnitude  $\text{MAG\_AUTO} < 24.0$  from the GOODS ACS  $i_{F775W}$  source catalogues (v1.1; detections based on the  $z_{F850LP}$  band).<sup>1</sup> We use hereafter elliptical apertures for each galaxy, adopting the source centre and ellipse shape (position angle and ellipticity) as given in the catalogues, keeping it fixed throughout the process. Several objects missed by the GOODS detection, presumably due to proximity of a bright neighbouring source, were inserted manually, using Source Extractor (Bertin & Arnouts 1996) to determine their shape. This initial sample contains 7,462 objects (3,992 in GOODS-North and 3,470 in GOODS-South).

The GOODS ACS images suffer from residual (i.e. non-zero) background flux, which typically reaches a level of 1/5 of the noise RMS in the  $i_{F775W}$  band. This background, along with a value of the noise RMS, was determined individually for each galaxy as a single value that corresponds to the median pixel value within a  $21'' \times 21''$ -box, applying five iterations of clipping outliers at 2.3 standard deviations. All sources were masked in this process, using 2.0 times the KRON\_RADIUS, taken from the official GOODS catalogues.

Proper masking of neighbouring galaxies is crucial for a reliable determination of the Petrosian radius (Petrosian 1976). On the one hand, object masks should be large enough to cover all contaminating light of close neighbours. On the other hand, if neighbour masks are too large they could encompass a big part of the target galaxy, rendering unreliable estimates of the Petrosian Radius.

After testing several ways to define the masks – e.g. using the KRON\_RADIUS or a preliminary Petrosian radius – we adopted an elliptical aperture that extends out to a surface brightness corresponding to one half of the local noise RMS (“half-noise semimajor axis” or “half-noise SMA”). In addition, we apply an iterative outlier clipping procedure in the surface brightness calculations used to determine the Petrosian radius, as described below. In the determination of the half-noise SMA, initial object masks were used that were based on the KRON\_RADIUS from the catalogues.

For each galaxy, we define a “Petrosian semimajor axis” (hereafter Petrosian SMA,  $a_{\text{Petro}}$ ), i.e., in the calculation of the Petrosian radius, we use ellipses instead of circles (cf. Lotz et al. 2004; Lisker et al. 2007). As mentioned above, the elliptical shape and

<sup>1</sup> <http://archive.stsci.edu/pub/hlsp/goods/>

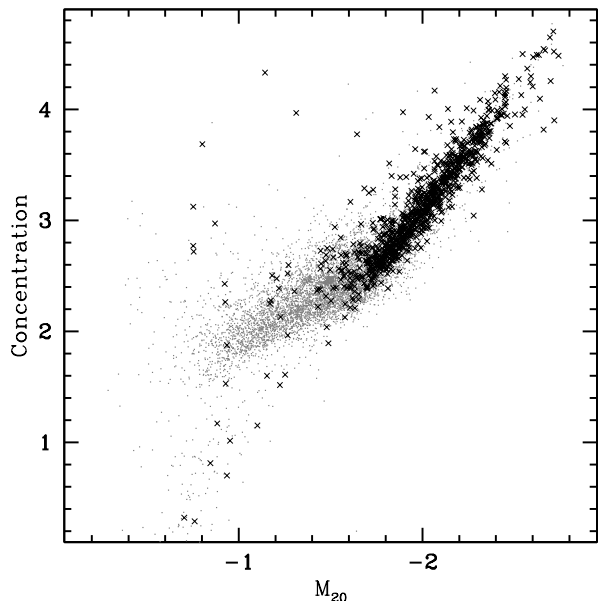


**Figure 1.** Distribution of concentration, as defined in Bershady et al. (2000) and  $M_{20}$  for all galaxies with  $i_{F775W} \leq 24$  (grey dots). Our final – visually classified – sample of early-type galaxies in the GOODS North and South fields is shown as black crosses. At the top-right corner C and  $M_{20}$  correspond to a one-component distribution with a high Sersic index. Towards the lower left corner, the contribution of a second component (i.e. a disk) makes  $M_{20}$  increase faster than C, resulting in a change of slope.

source centre of each object were taken from the GOODS official catalogues, and kept fixed during the process. The Petrosian SMA was defined as the semimajor axis  $a$  at which the local intensity falls below one fifth of the average intensity within  $a$ . The local intensity is measured as the average intensity within an elliptical annulus reaching from  $0.9a$  to  $1.1a$ , applying five iterations of clipping outlying pixel values at 2.3 standard deviations. Neighbouring objects were masked using the half-noise SMA, or the KRON\_RADIUS for sources with  $MAG\_AUTO \geq 24.0$ . For 250 objects (3.4%), a neighbouring source was so close that its mask encompassed the centre of the target galaxy, rendering a Petrosian SMA derivation impossible. For another 72 objects (1.0%), the derived Petrosian SMA is clearly too large from visual inspection, in most cases caused by diffuse light or background inhomogeneities.

To obtain the total magnitude, effective radius, and effective surface brightness of each galaxy, we measured the  $i_{F775W}$  flux within  $a = 1.5 a_{\text{Petro}}$ , and the semimajor axis containing 50% and 90% of this flux ( $a_{50}$  and  $a_{90}$ , respectively). For galaxy images affected by a neighbour mask – therefore without a Petrosian SMA – we used the KRON\_RADIUS instead of  $a = 1.5 a_{\text{Petro}}$ , and performed no masking of neighbours. For those whose Petrosian SMA was found to be too large, we also adopted the KRON\_RADIUS, but did mask neighbouring galaxies. From a comparison of catalog magnitudes ( $MAG\_AUTO$ ) with final magnitudes ( $m_i$ ) for our early types, we find that for 3-4% of the objects, the final magnitude is brighter by more than 0.5 mag than the catalog magnitude. Based on our preselection of galaxies with  $MAG\_AUTO < 24.0$ , we estimate our completeness to be 95% at  $m_i \leq 23.5$  mag.

The flux lost due to masked areas within the aperture was corrected by assigning the azimuthally averaged intensity to the masked pixels. We then applied a correction to the estimate of half-

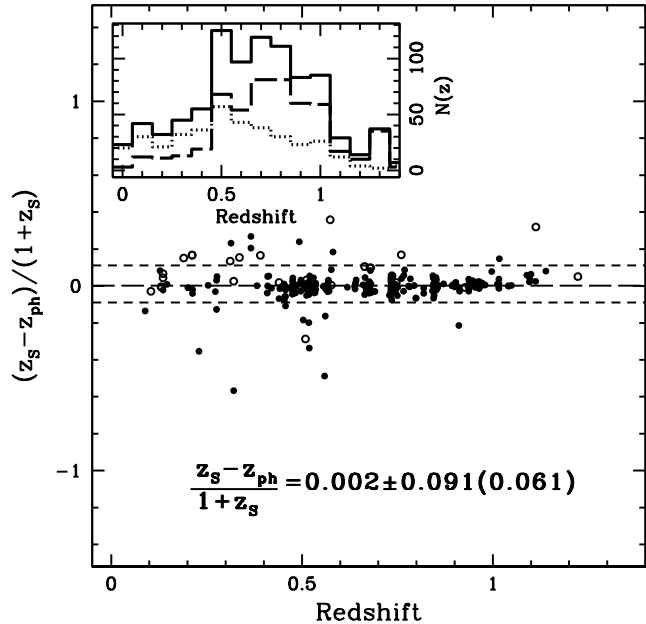


**Figure 2.** Comparison between our photometric redshifts and published spectroscopic redshifts (see text for details). Solid (open) circles correspond to photometric early (late) types. The comparison is restricted to galaxies with  $i_{F775W} < 23$  (with the full sample down to  $i_{F775W} < 24$ , the standard deviation of the comparison is 0.13). The long (short) dashed lines show the sample mean (rms). The rms given in brackets correspond to the scatter when  $3\sigma$  outliers are removed from the sample. Inset: Redshift distribution of the complete sample (both North and South fields; thick solid line), using spectroscopic redshifts where available. The other histograms split the sample into photometric early- (dashed line) and late-types (dotted line).

light radius and apparent magnitude. This correction was obtained from simulations of galaxies with Sersic surface brightness profiles and realistic noise obtained from the GOODS/ACS weight maps. Notice that this correction fixes two different effects: the dominant one in this case comes from the fact that the apparent sizes are close to the resolution limit of the observations. The second correction is required as light measured within an aperture will lose flux, and this loss is related to the steepness of the surface brightness profile (see e.g. Graham & Driver 2005; Graham et al. 2005). Our simulations show that the correction can be written as a function of two observables: the dominant one is the estimated  $R_e$  and the second order one is the concentration, measured as  $R_{90}/R_{50}$  (see appendix A for details).

The simulations allow us to assess the accuracy of the retrieved size, magnitude and apparent surface brightness. Four mock samples of 910 galaxies each were generated with the same values of  $i_{F775W}$  and  $R_e$  as the real sample. These galaxies were given a random eccentricity  $0 < e < 0.6$ , position angle, and Sersic (1968) index  $2 < n < 4$ . We could successfully retrieve the half-light radius with an accuracy of 9%, the  $i_{F775W}$ -band total apparent magnitude within 0.05 mag, and the average  $i_{F775W}$ -band surface brightness within the half-light radius to within  $0.16 \text{ mag/arcsec}^2$  (see appendix A for details).

## 2.2 Morphological Classification

Galaxy morphology studies (e.g. Abraham et al. 1994; Lotz et al. 2004; Menanteau et al. 2004; Scarlata et al. 2007) still lack a re-

liable classification method in an unsupervised way with acceptable levels of contamination and completeness. Currently, all these methods always require visual inspection. We decided to tackle the selection of early-types only by visual inspection. The South field sample of early-types was taken from Ferreras et al. (2005), with a total of 377 early-type galaxies, out of a total of 3,470 galaxies at  $i_{F775W} < 24$  (10.9%). For the North field we follow an identical procedure. All sources brighter than  $i_{F775W} = 24$  mag are inspected by the four authors of this paper. We use  $ds^2$  to view each galaxy in all four bands. After a first selection, we accept an early-type galaxy if classified as such by at least three of us. A second pass of visual inspection by the same people follows, this time restricted to the list of galaxies already labelled during the first pass as early-types by one or two of us. Galaxies classified as early-types by three of us in this second pass are added to the final sample. Out of 3,992 sources in the North field, we selected 533 galaxies (13.4%), with a total in both fields of 910 galaxies. The different fraction is compatible within Poisson statistics. Furthermore, Cosmic Variance will certainly have an effect on the discrepancy between the North and South fields.

Two “non-parametric” measures of galaxy morphology are shown in Fig. 1 for our sample: the concentration index ( $C$  Bershady et al. 2000), and the  $M_{20}$  parameter (Lotz et al. 2004).  $C = 5 \log R_{80}/R_{20}$ , where  $R_X$  is defined as the radius within which one has  $X$  percent of the total flux.  $M_{20}$  is the normalized second-order moment of the brightest 20% of galaxy pixels (*no matter where they are*), and thus quantifies whether these pixels are confined to a small region or widely spread. The figure, analogous to Fig. 1 in Ferreras et al. (2005), shows that the majority of galaxies follow a well-defined relation in the  $C$ - $M_{20}$ -plane, which consists of two linear parts with different slope. The change in slope marks the transition between bulge-dominated and disk-dominated or irregular objects: for the former, the brightest 20% of pixels are fully located in the centre, whereas for the latter, a growing fraction is located outside of the central region.

### 2.3 Redshift and Rest-frame Estimates

We retrieved the latest publicly available spectroscopic redshift catalogues from the GOODS fields: FORS2 (Vanzella et al. 2008) and VVDS (Popesso et al. 2008) in CDFS and the Team Keck Redshift Survey (Wirth et al. 2004) in HDFN. In Ferreras et al. (2005) photometric redshifts were taken from Mobasher et al. (2004) for galaxies without a spectroscopic measurement. In this paper we determine our own photometric redshifts both in the North and South fields for consistency. Our code is based on a template fitting technique without any priors and uses a set of eight templates built from Bruzual & Charlot (2003) population synthesis models. Each template is a  $\tau$ -model, i.e. a composite stellar population at solar metallicity with an exponentially decaying star formation rate ( $\tau$ ). We fix the formation redshift  $z_F=3$  for all templates, with timescales:  $\tau = \{0.05, 0.5, 1.0, 2.0, 4.0, 5.0, 6.0, 8.0\}$  Gyr. We label these star formation histories with an integer  $t=\{0, \dots, 7\}$ . The templates are transformed according to a Fitzpatrick (1999) law for Galactic reddening with a colour excess  $E(B-V)=0.012$  (HDFN) and 0.010 (CDFS), values taken from Schlegel et al. (1998) for the central positions of both fields. Each model is run over a range of redshifts out to  $z=3$  with the available photometry estimated over a

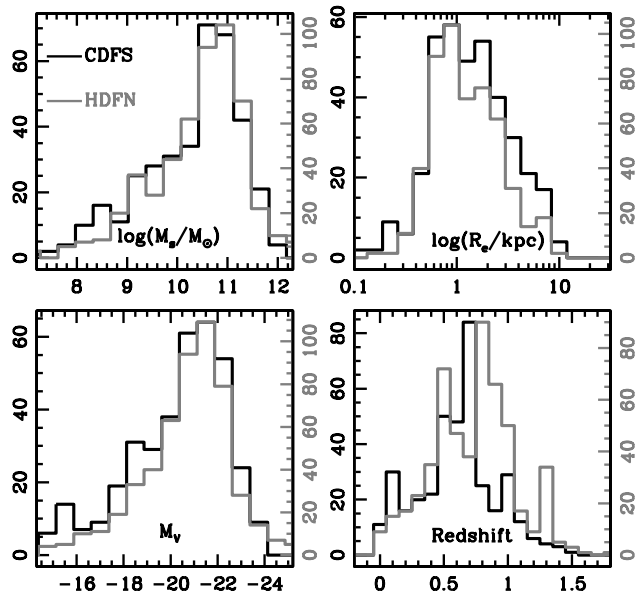


**Figure 3.** Distribution of various observables. The histograms separate between the North (grey) and the South (black) fields in order to illustrate the effect of Cosmic Variance.

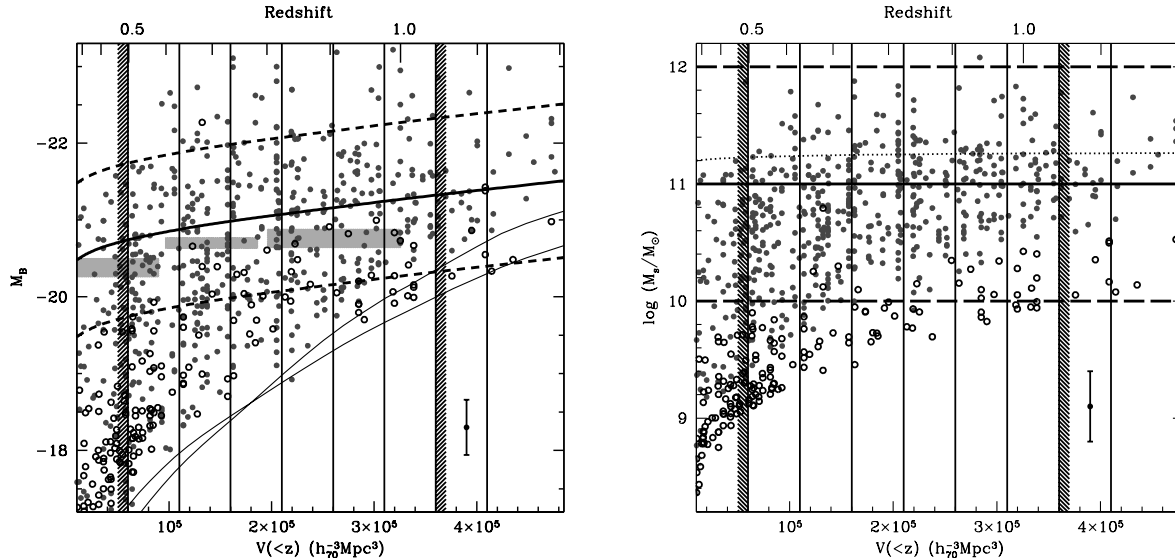
fixed aperture. The photometry comes from the GOODS/ACS images ( $B, V, i, z$ ) and is directly extracted from the publicly available v2.0 images. For HDFN we also include ground-based photometry from Capak et al. (2004); which includes KPNO/4m  $U$ -band and UH/2.2m  $HK'$  data. In CDFS optical and NIR photometry is taken from WFI/NTT and ISAAC/VLT as used in the photometric redshift catalogue of Mobasher et al. (2004).

Figure 2 shows a comparison of photometric and spectroscopic redshifts for galaxies brighter than  $i_{F775W} < 23$ . The average (0.002) and scatter (0.091) of the discrepancy – measured as  $\Delta z/(1+z_S)$  – is comparable to the best redshift estimates available (Mobasher et al. 2004, 2007). If outliers at the  $3\sigma$  level are removed from the sample, the scatter reduces to 0.061. The fraction of outliers is 2.9% with no significant dependence on galaxy type.

Our photometric redshift code also identifies each galaxy with the template that gives the best fit. This allows us to split the sample into “photometric” red and blue galaxies depending on whether the best fit corresponds to old or younger stellar populations. We compared this new classification – using the templates presented above – with those done in Ferreras et al. (2005), which were based on the photometric types from Mobasher et al. (2004). In this paper we choose the separation between photometric red and blue ellipticals at the third template ( $t=2$ ): all galaxies which are best fit by an exponential timescale of 1 Gyr or shorter are considered “red” throughout this paper. With this choice, the number of “red” early-type galaxies in the total sample is 670 ( $\sim 75\%$ ). The fraction of red early-types in the North and South fields is 375/533 and 295/377, compatible within Poisson error bars.

In addition, we used redshifts determined for a subsample of our dataset, for which IF and AP have access to ACS/HST slitless grism spectroscopy (G800L) from the PEARS project (Probing Evolution And Reionization Spectroscopically; PI S. Malhotra; HST Proposal ID # 10530) The low-resolution spectra ( $R \sim 50 - 80$ ) allowed us to secure redshifts with comparable accu-

<sup>2</sup> <http://hea-www.harvard.edu/RD/ds9/>



**Figure 4.** Redshift evolution of the comoving number density: The  $B$ -band absolute magnitude (left) and stellar mass (right) is compared with  $V(<z)$ , i.e. the comoving volume within a given redshift (the redshift appears in the top axis). Vertical lines delimit redshift bins used in the analysis of the number density in the next figure, with the upper and lower limits shown as shaded regions. Galaxies are shown as grey dots (photometric early-type) or open circles (late-type). The curved, thin solid lines in the left panel are the limiting  $i_{F775W} = 24$  for a photometric early- or late-type. The thick line and dashed lines above and below illustrate the sample separation into “bright” and “faint” subsets (or high and low stellar mass in the right panel; see text for details). Grey areas in the left panel are  $L_*$  values from Ilbert et al. (2006). The dashed line in the mass plot follows  $M_*$  from Fontana et al. (2006).

racy to the spectroscopic ones because of the prominent  $4000\text{\AA}$  break found in most of these galaxies. For details we refer the interested reader to the paper on the analysis of the grism data from the GOODS early-types (Ferrerias et al., in preparation), or to a similar study on the HUDF (Pasquali et al. 2006). Out of the total sample of 910 early-type galaxies in this paper, we have spectroscopic or grism-based redshifts for 541 galaxies. Hence, 59.5% of the total sample have spectroscopically accurate redshifts.

The redshifts are used to determine rest-frame properties of the galaxies. The physical projected half-light radius is determined by using the angular diameter distance for a *concordance* cosmology, namely  $\Omega_m = 0.3$ ,  $\Omega_\Lambda = 0.7$  and  $H_0 = 72$  km/s/Mpc. The best fit template is compared to the apparent total magnitude to estimate the absolute magnitude and stellar mass – a Chabrier (2003) Initial Mass Function is used throughout this paper. From the ACS  $B$  (where available),  $V$ ,  $i$ ,  $z$  photometry we choose the passband with the lowest  $K$ -correction for the transformation into absolute magnitude. As an estimate of the amount of correction applied, the RMS of the  $K$ -corrections for the full sample is 0.42 mag for  $M_B$  and 0.27 mag for  $M_V$ . Regarding stellar mass estimates, even though the age and metallicity distribution of a composite stellar population cannot be constrained with broadband photometry, the stellar mass can be reliably constrained to within 0.2 – 0.3 dex provided the adopted IMF gives an accurate representation of the true initial mass function (see e.g. Ferreras, Saha & Burles 2008). In order to assess the effect of the passband on the determination of stellar mass we compare our stellar masses – based on  $i_{F775W}$  – with the  $K_s$  photometry of the CDFS field from ISAAC/*VLT* (Retzlaff et al., in preparation). Over the redshift range probed by our sample,  $i$ -band and NIR mass estimates differ by less than 0.15 dex (see appendix B).

Figure 3 shows the distribution of stellar mass, projected phys-

**Table 1.** The sample of early-type galaxies ( $i_{F775W} < 24$ )

Sample	Number	$f_B^a$	$z^b$	$M_s^b (M_\odot)$	$M_V^b$	$R_e^b$ (kpc)
HDFN	533	0.30	0.78	$4.2 \cdot 10^{10}$	-20.9	1.10
CDFS	377	0.22	0.64	$3.3 \cdot 10^{10}$	-20.6	1.26
All	910	0.26	0.68	$3.7 \cdot 10^{10}$	-20.8	1.15
S1 <sup>c</sup>	411	0.04	0.85	$1.2 \cdot 10^{11}$	-21.9	2.11
S2 <sup>c</sup>	280	0.11	0.56	$3.4 \cdot 10^{10}$	-20.6	1.55

<sup>a</sup> Blue early-type fraction: Red/Blue types selected from photometric redshift best type (Red:  $t \leq 2$ , i.e. star formation timescale  $\tau \leq 1$  Gyr, see text for details). <sup>b</sup> Median value. <sup>c</sup> S1 and S2 are volume-limited subsamples, defined in §4.

ical size, absolute magnitude and redshift. The sample is shown separately for the North (grey) and South (black) fields. Both fields have a similar range in mass or size, but the redshift distribution illustrates the effect of cosmic variance over the individual  $160$  arcmin<sup>2</sup> areas. The variation in the total number of early-type galaxies (533 in the North vs. 377 in the South) is also caused by such effect (the selection method being identical in both fields). Some of the basic properties of this sample is shown in table 1. The table also shows the properties of a couple of volume-limited subsamples (S1 and S2) defined in §4.

### 3 NUMBER DENSITY EVOLUTION: LUMINOSITY VS. MASS

A simple way to assess the redshift evolution in the number density of early-type galaxies is illustrated in figure 4, where the  $B$ -

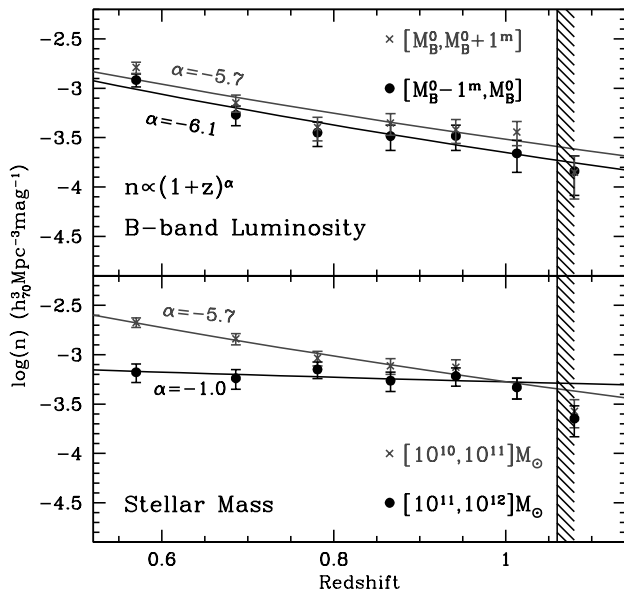


**Figure 5.** Redshift evolution of the top end of the mass and luminosity distribution as illustrated in the previous figure. The black dots correspond to the brighter (top panel) or more massive (bottom) subsample. The fainter subsample is shown as grey crosses. Error bars include Poisson noise and the uncertainty in the K-correction. The lines give fits to a power law, with index  $\alpha$ , which is labelled for all subsamples.

band absolute magnitude (*left*) or stellar mass (*right*) is presented with respect to the comoving volume enclosed within the redshift of each galaxy. Hence, counting galaxies within cells in this figure gives the comoving number density at a given redshift. The thin solid lines track the flux limit imposed by our search ( $i_{AB} < 24$ ). This limit depends on the K-correction adopted, thereby we show in the figure the absolute magnitude limit taking the extrema of the templates used in the photometric redshift analysis (i.e. types  $t=0$  and  $t=7$ ). Galaxies are shown according to the convention adopted throughout this paper, namely red galaxies as grey solid dots (photometric type  $t \leq 2$ ) and blue galaxies as black open circles ( $t > 2$ ). In both cases – absolute magnitude and stellar mass – we split the sample in two bins. In absolute magnitude we define 1 mag bins (dashed lines) above and below a typical  $L_*$  galaxy represented by the thick solid line, which corresponds to  $M_B^0 \sim -21$ . In order to track its evolution with redshift, we assume an exponential star formation history with formation redshift  $z_F=5$ , timescale  $\tau_{SF} = 0.5$  Gyr and solar metallicity. For comparison, the shaded boxes delimit the value of the  $M_B^*$  Schechter fits of the VIMOS-VLT Deep Survey for early-type galaxies (Ilbert et al. 2006). We decided to choose this binning criterion instead of a fixed absolute magnitude in order to overcome the passive fading of the stellar populations. The shaded areas show that our low-luminosity bin roughly maps  $L_*$  galaxies.

Regarding stellar mass, we choose a fixed reference mass ( $10^{11} M_\odot$ ; thick solid line). The sample is split in 1 dex bins above and below this reference (dashed lines). For reference, the dotted line tracks the characteristic stellar mass scale of Fontana et al. (2006). A typical error bar is shown in both panels. The vertical lines in both panels mark the redshift bins, with the full range for a complete volume-limited sample given by the hatched vertical regions.

Figure 5 shows the evolution in comoving number density with respect to absolute magnitude (*top*) or stellar mass (*bottom*) obtained from the previous diagram. The error bars are estimated from a sum in quadrature of the Poisson noise in each bin and the uncertainty in the absolute magnitude or mass. This uncertainty is computed using a Monte Carlo algorithm in which noise is added to the absolute magnitude or stellar mass of each galaxy. 5,000 realizations are generated and each is analysed in the same way as our original sample. The error bars give the standard deviation within the ensemble. The evolution of the number density can be modelled by a simple power law  $n \propto (1+z)^\alpha$ . In luminosity there is no significant difference between the “bright” and “faint” subsamples. However, the most massive galaxies show a remarkable weak trend with redshift, with a slope significantly different to less massive galaxies. With the adopted fits to the data, an extrapolation to lower redshift yields a decrease of a factor  $\sim 50$  in the number density of early-type galaxies between  $z=0$  and  $z=1$  for the mass range  $10^{10} - 10^{11} M_\odot$ ; whereas the decrease is just a factor 2 for galaxies with stellar masses between  $10^{11}$  and  $10^{12} M_\odot$ . This result is presented in more detail in a letter (Ferreras et al. 2008) where we show that this result is in agreement with recent work in other surveys (e.g. Conselice et al. 2007) and with recent semi-analytic models of galaxy formation (e.g. Khochfar & Silk 2006).

#### 4 INTRINSIC COLOUR DISTRIBUTION

The *internal* colour distribution of a galaxy can reveal important information regarding its star formation and assembly history. Early-type galaxies have smooth surface brightness distributions, which make them ideal targets for this sort of study in GOODS. For each colour map three pieces of information can be gathered in a robust way: the average colour within an aperture (the projected half-light radius in our case); the radial gradient of the colour distribution, and the scatter about the best fit (assumed to be linear between colour and  $\log R$ ). We follow the same technique as described in Ferreras et al. (2005), briefly outlined here.

The colour map is generated by convolving the image taken in one filter with the Point Spread Function (PSF) of the other filter used to define the colour. This is the most robust way to reduce the colour trends caused by a different resolution between images in different bandpasses. We used a PSF generated from stellar images in the same dataset. Ferreras et al. (2005) includes an appendix that shows the – negligible – difference in the colour gradients and scatter when using either a stellar image from the same data or a synthetic PSF generated by TinyTimKrist (1993).

The images span a wide range of signal-to-noise ratios on a pixel-by-pixel basis. Hence, it is best to bin the pixels although preserving spatial information as much as possible. A Voronoi tessellation method was adopted, in which a target S/N is specified so that the algorithm merges nearby pixels into tiles, keeping these tiles as round as possible, following the algorithm by Cappellari & Copin (2003). The process is finished when a target S/N *per tile* is reached. In Ferreras et al. (2005) we showed that estimates of radial colour profiles are much improved as the outer parts of the galaxy have a significantly lower noise after a Voronoi tessellation. We impose a target S/N=10 per tile for each colour. The radial distribution of colour vs  $\log R/R_e$  is fit to a straight line. We also determine the colour scatter about this best fit by using a biweight estimate (Beers et al. 1990).

The left panel of figure 6 shows the *observer frame*  $V - i$  colour distribution as a function of redshift, half-light radius and

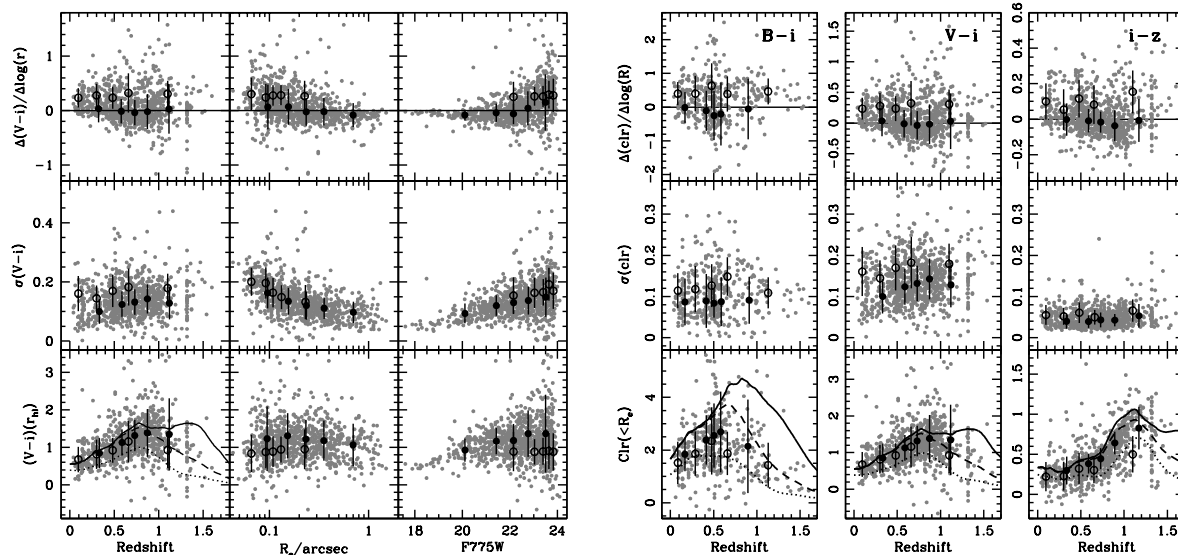


**Figure 6.** *Left:* The observer-frame colour gradient (*top*), scatter (*middle*), and integrated colour within the half-light radius (*bottom*) are shown with respect to three observables: redshift (*left*); apparent half-light radius (*middle*) and  $i_{F775W}$  apparent magnitude (*right*). The full sample is shown in grey. Black points correspond to average values of subsamples (after a  $5\sigma$  clipping) binned at constant number of galaxies per bin, and separated with respect to the best fit populations: old (filled dots; photometric type  $t \leq 2$ ) and young (hollow dots;  $t > 2$ ). *Right:* Redshift evolution of the intrinsic distribution of the three available colours, as labelled. In both figures the lines in the bottom panels correspond to the evolution of a set of exponentially decaying star formation histories with solar metallicity, started at  $z_F=5$  with a decay timescale of 0.5 (solid line) 1 (dashed line) and 8 Gyr (dotted line).

apparent  $i$  band magnitude of the whole sample (grey dots). The larger dots correspond to binning the sample at a fixed number of galaxies per bin, separating them in photometric type between red ( $t \leq 2$ ; solid circles) and blue ( $t > 2$ ; hollow dots). Error bars represent the standard deviation within each bin. For comparison, the lines at the bottom-left corner track exponentially decaying star formation histories at solar metallicity with formation redshift  $z_F=5$  and timescales  $\tau = 0.5$  Gyr (solid), 1 Gyr (dashed) and 8 Gyr (dotted).

In the top panels, the radial colour gradient is shown. Galaxies with red (blue) cores have negative (positive) gradients. We obtain a consistent result with respect to Ferreras et al. (2005). Galaxies with blue cores are almost always photometrically classified as “blue” and galaxies with red cores are classified as “red”. This is not a trivial statement, as the overall colour of the galaxy need not correlate with the radial gradient. The scatter does not correlate with redshift, but there is a clear trend with size or apparent magnitude. This can be caused by a combination of physical and passband-shifting effects and we defer the discussion to a later figure.

On the right side of figure 6, a similar plot is presented for the three available colours from the ACS images. The  $B-i$ ,  $V-i$  and  $i-z$  colour distributions are shown with respect to redshift. The lines in the bottom panels correspond to the same models as in the left side of the figure. The trend is consistent with all three colours, with blue galaxies having positive colour gradients.

In order to extract meaningful trends of the intrinsic colour distributions we have to define volume-limited subsamples that will remove biases inherent to flux-limited samples. Figure 7 illustrates our selection process. The complete sample is shown in absolute magnitude vs redshift space. The distribution shows the characteristic boundary caused by the  $i_{F775W} = 24$  limit. The solid line

tracks a  $i_{F775W} = 24$  galaxy as a function of redshift, assuming a typical star formation history for an early-type galaxy (photometric type  $t=1$ ). A compromise has to be made when generating volume-limited samples: either we probe as deep as possible in redshift – cutting in absolute magnitude, and thereby sacrificing faint galaxies, or we probe as faint as possible the luminosity function – cutting in redshift. In order to explore these two choices we select two subsamples, shown as black dots in each panel: S1 (412 galaxies; *left*) is a sample targeted to explore the redshift evolution, and is restricted to galaxies brighter than  $M_V < -21$ . We also apply a cut in redshift ( $z < 1.4$ ). Subsample S2 (280 galaxies; *right*) targets a wide range of luminosities out to  $z < 0.7$ . In this case the volume-limited sample extends to fainter galaxies  $M_V < -19$ . The bottom panels of figure 7 show the histograms in stellar mass (*left*) and projected physical size of each subsample.

Figure 8 focuses on the redshift evolution of the colour distribution and shows the observer-frame  $V-i$  colour gradient (*top*) and scatter of subsample S1. For comparison, the colour gradients observed in a sample of moderate redshift clusters by Tamura & Ohta (2000) is shown as stars. Our sample is shown with the usual coding with respect to photometric type: red (grey dots) and blue (open circles). In the appendix of Ferreras et al. (2005) simulations of galaxies with the same characteristics as the GOODS galaxies were done to show that from photometric errors one could expect a typical colour scatter  $\sigma(V-i) \lesssim 0.03$  mag, with a maximum of 0.05 mag for the faintest galaxies. Figure 15 in the appendix of Ferreras et al. (2005) shows that both the observed scatter and slope are intrinsic.

We include in the figure a simple model prediction which uses the local  $B-R$  colour gradients of elliptical galaxies in the local Universe as constraint (Peletier 1990). The set of two nearly horizontal lines – just below the  $\Delta(V-i)/\Delta\log(R) = 0$  axis – assumes the  $z=0$  intrinsic colour gradient to be caused by a pure

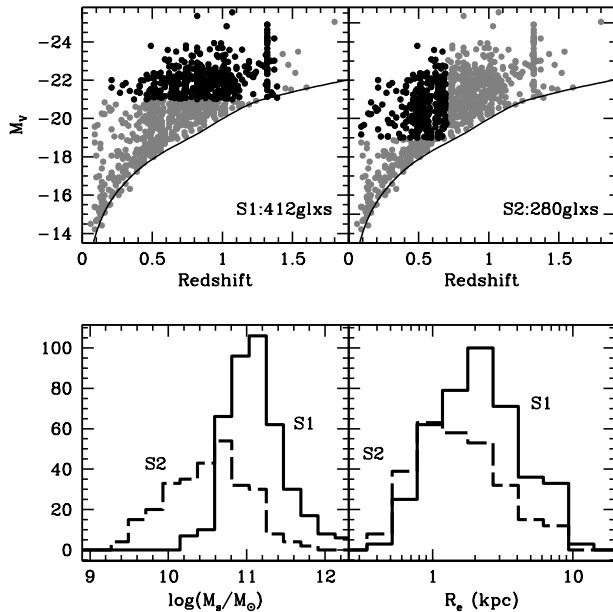


**Figure 7.** Volume limited subsamples of early-type galaxies in GOODS N+S fields. S1 focuses on massive systems out to redshift  $z < 1.4$ , whereas S2 limits the redshift out to  $z < 0.7$  in order to maximise the range of masses/luminosities. The top panels show  $V$ -band absolute magnitude vs redshift, with the  $i_{F775W} < 24$  flux limit shown as a solid line. The bottom panels show the histograms of each subsample in stellar mass and projected size.

metallicity sequence, i.e. we fix an age throughout the galaxy and compute the difference in metallicity that will give the observed colour gradient in local early-type galaxies. Then we evolve this model backwards in time to assess the evolution in the colour gradient. Standard models with exponentially decaying star formation histories are used for the fit. The timescale is fixed at  $\tau = 1$  Gyr and the formation epoch is either  $z_F=2$  (solid line) or 5 (dashed line). The second sets of models – which curve down at  $z < 0.6$  – assume a pure age sequence for the colour gradient at fixed (solar) metallicity, with a similar set of models (in this case the bluer outer region is modelled by a slightly longer star formation timescale). As expected, this model gets very steep with increasing redshift because of the strong dependence of colour with age. A third model (dotted line) overlays on top of a metallicity sequence formed at  $z_F=5$  a second, younger stellar population *in the core*, formed at  $z=0.8$ . This younger component contributes only 10% in mass, illustrating the effect that a small episode caused by a minor merger would have on the colour gradient.

This result illustrates that blue cores have a radial range of ages, being youngest at their centres. The large blue colour gradients observed in many of the blue cores cannot be explained by an “inverted” gradient in metallicity, i.e. more metal-rich populations outwards. If we were to explain the large range in colour between the inner and the outer parts of the galaxy by metallicity alone, one would have to invoke unrealistically low metallicities at the galaxy centre. Furthermore, this scenario would predict no redshift dependence on the fractional contribution of blue cores, in contrast to the observations. In this subsample (S1) of luminous ( $M_V < -21$ ) early-type galaxies, the median redshift of blue and red early-types is 1.10 and 0.85, respectively, i.e. bluer early-type galaxies (at least at the massive end) contribute more significantly at  $z \gtrsim 1$ .

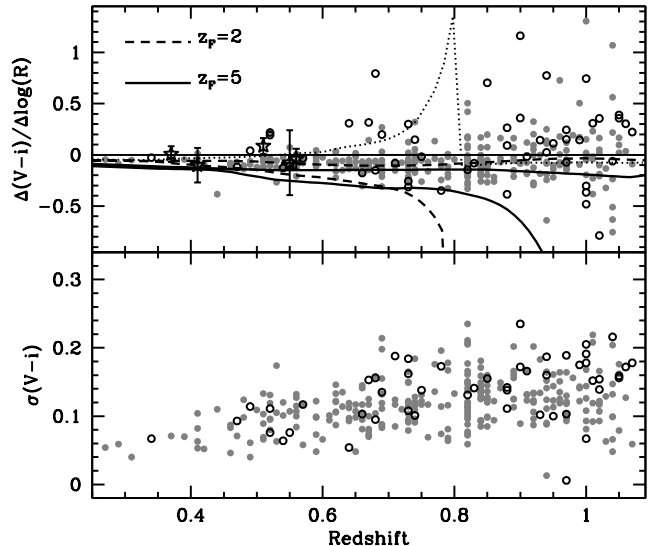


**Figure 8.** Intrinsic  $V - i$  colour distribution of subsample S1: The slope (top) and scatter of the radial colour gradient is shown with respect to redshift. The sample is separated into photometric early- (grey dots) and late-types (open circles). Stars are gradient measurements in a sample of cluster early-types from Tamura & Ohta (2000). Two alternative models for the evolution of the colour gradient are shown, depending on whether the gradient is caused by metallicity (thin, nearly horizontal lines) or age (thick, curved lines). Two formation redshifts are considered for each case:  $z_F=5$  (solid lines) or 2 (dashed lines). The dotted line corresponds to a metallicity sequence with formation redshift  $z_F=5$ , adding to the core 10% (in mass) of a stellar population formed at  $z=0.8$ .

The relation between colour distribution and galaxy properties is explored in figure 9; where the colour gradient (top) and scatter is shown with respect to stellar mass; projected half-light radius and  $V$ -band absolute magnitude for subsample S2. Blue cores typically have stellar masses below  $10^{10} M_\odot$  and half-light radii  $R_e \lesssim 1$  kpc, a signature of downsizing. In this subsample the average stellar mass of the blue ellipticals is  $5 \cdot 10^9 M_\odot$  compared to  $4 \cdot 10^{10} M_\odot$  for red ellipticals. This strong mass-dependence suggests that AGN activity alone is not enough to explain the blue cores (Menanteau et al. 2005).

## 5 THE KORMENDY RELATION

The Kormendy relation (hereafter KR; Kormendy 1977) is a tight linear correlation between average surface brightness – typically measured within the half-light radius ( $R_e$ ) – and the logarithm of  $R_e$ . It is one of the projections of the Fundamental Plane (Djorgovski & Davis 1987), which relates surface brightness, size and velocity dispersion. The Fundamental Plane and its projections are a consequence of the dynamics of early-type galaxies and their underlying stellar populations. KR is therefore the “next best thing” to the Fundamental Plane when measurements of velocity dispersion are not available. The observed dispersion of the KR at  $z=0$  is  $\sim 0.4$  mag arcsec $^{-2}$  (La Barbera et al. 2003). The redshift evolution of the Kormendy relation can be used to constrain the assembly and formation history. A significant change in slope with redshift can reveal the presence of star formation or the rearrangement of the stars because of “dynamical activity” (i.e. mergers).

Figure 10 shows the Kormendy relation of both volume-limited samples S1 and S2 (grey dots). The surface brightness is

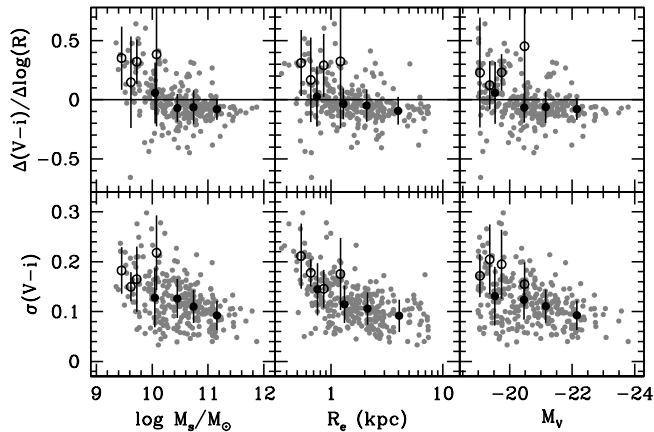


**Figure 9.** Intrinsic ( $V - i$ ) colour distribution of subsample S2: The slope (top) and scatter of the observed  $V - i$  colour distribution – roughly rest-frame  $B - V$  over the redshift range of S2 – is shown with respect to stellar mass (left); projected half-light radius (middle) and  $V$ -band absolute magnitude (right). The black points with error bars correspond to average values of subsamples separated with respect to photometric redshift type: old (filled dots; type  $t \leq 2$ ) and young (hollow dots;  $t > 2$ ).  $1\sigma$  error bars are shown (after a  $5\sigma$  clipping). The binning is done at constant number of galaxies per bin.

computed as the average within the half-light radius. Open black dots correspond to the upper quartile in redshift (S1, left) or stellar mass (S2, right), as labelled. The solid line is the local relation observed in the Coma cluster (Jørgensen et al. 1995) and the crosses are a sample of 17 galaxies from the K20 survey (di Serego Alighieri et al. 2005). Sample S1 – which extends to higher redshift than S2 – has a significantly brighter zero point, caused by the effect of lookback time on the stellar populations. For comparison, a simple stellar population formed at  $z_F=5$  and solar metallicity undergoes a fading of  $\sim 1$  mag in the rest-frame  $B$  band between redshifts  $z=1$  and 0, similar to the offset found in the left panel of figure 10. Sample S2 (right) has a KR compatible with local early-type galaxies (again with a significant shift of the zero point caused by lookback time). As expected, galaxies with a higher stellar mass content appear brighter than less massive galaxies with the same size, roughly a direct consequence of a non-homologous surface brightness distribution (Graham & Guzmán 2003). An estimate of the typical error bar is shown in each panel. For the surface brightness we use the scatter of the K-corrections applied to obtain  $B$ -band magnitudes (0.4 mag). The true error should be most certainly smaller than this K-correction. The error in the size is taken from the worst case scenario when retrieving half-light radii from simulations (see appendix). The K20 sample from di Serego Alighieri et al. (2005) (crosses) span a narrow redshift range ( $0.9 \cdot \cdot 1.3$ ), and are compatible with our high-redshift (left) or massive (right) subsamples.

Notice the major difference between the selection criterion of this work and Ferreras et al. (2005). In that paper, a Kormendy selection was imposed on the visually classified sample, so that early-types that were found not to evolve into the local KR were rejected from the sample. In that case, a large number of low-redshift, blue early-types were rejected. It was discussed whether misclassification of bright knots of star formation or an active nucleus could explain this rejection. In this paper we use visual classification as the only selection criterion. We later define volume-limited subsamples. In this process we end up rejecting similar type of galaxies as

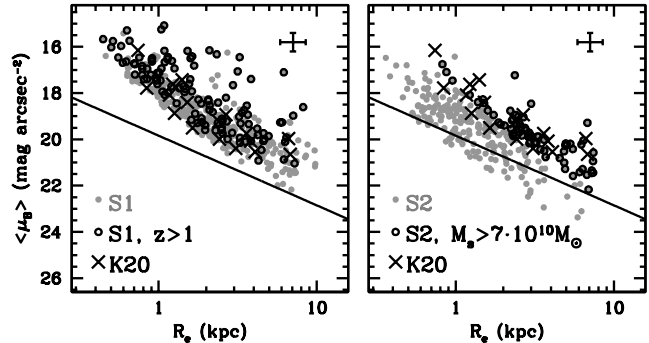


**Figure 10.** Kormendy relation of samples S1 (left) and S2 (right) in the rest-frame  $B$ -band (grey dots). Open circles dots are the upper quartile of the redshift (S1) or the stellar mass distribution (S2), as labelled. A typical error bar is shown. The data have been corrected for the  $(1+z)^4$  cosmological dimming. The line represents the local relation observed in the Coma cluster (Jørgensen et al. 1995). The 17 galaxies from the K20 sample are shown as crosses (di Serego Alighieri et al. 2005).

in Ferreras et al. (2005) for different reasons. Figure 4 shows that most of the faint, low-redshift galaxies in our sample are removed from S1 or S2 to enforce completeness. Those are mainly blue early-types with small sizes. The addition of those galaxies to S1 or S2 would result in significant scatter towards the bottom-left corner of the Kormendy relation in figure 10, in a similar fashion to the presence of the “dwarf galaxy branch” presented in the Kormendy Relation plot of Capaccioli et al. (1992). Hence we conclude that a significant fraction of the galaxies rejected in Ferreras et al. (2005) because of the KR constraint must be dwarf ellipticals at  $z \lesssim 0.4$ .

Figure 11 shows the redshift evolution of the KR of subsamples S1 and S2 in terms of slope (top); average surface brightness (middle) and scatter (bottom; using a biweight estimator). Sample S2 is split at the median value of stellar mass ( $3.5 \cdot 10^{10} M_\odot$ ). The fit is done with a standard least squares algorithm, binning the samples at constant number of galaxies per bin (hence the unequal separation between dots in the figure). The arrow in the top panel represents the  $z=0$  slope of the Kormendy Relation (La Barbera et al. 2003). Sample S1 (black dots) – focussing on bright galaxies out to the highest redshifts – shows a remarkable agreement with the local observations, and with moderate redshift clusters (Ziegler et al. 1999). We extend the conclusion of Ziegler et al. (1999) of a negligible change in the slope of the KR to a wide range of redshifts and to a field environment. The most massive galaxies in sample S2 (grey triangles) also agree with the local observations, whereas a selection of the galaxies with the lower masses in S2 (grey stars) have larger scatter and steeper slopes.

In the middle panel we compare the observed trend of the average surface brightness with the fading of a typical old population as labelled in the figure caption. Notice that the least massive galaxies of sample S2 are consistently brighter than this estimate, reflecting the presence of younger stellar populations. It is interesting to notice that the  $\sim 0.5$  mag arcsec $^{-2}$  scatter about the best fit (bottom) does not change significantly with redshift or sample.

To summarise, we find the Kormendy relation of  $z \sim 0.3 - 1.2$  to be the same as at  $z \sim 0$ . The slope and scatter of the correlation does not change and the zero point, i.e. the typical surface brightness changes in agreement with pure passive evolution. Only lower mass spheroidals ( $M_s < 3.5 \cdot 10^{10} M_\odot$ ) show a significant departure from the average  $z = 0$  Kormendy relation, appearing brighter in  $\langle \mu_B \rangle^0$  and with a steeper slope. We believe this result is caused by a

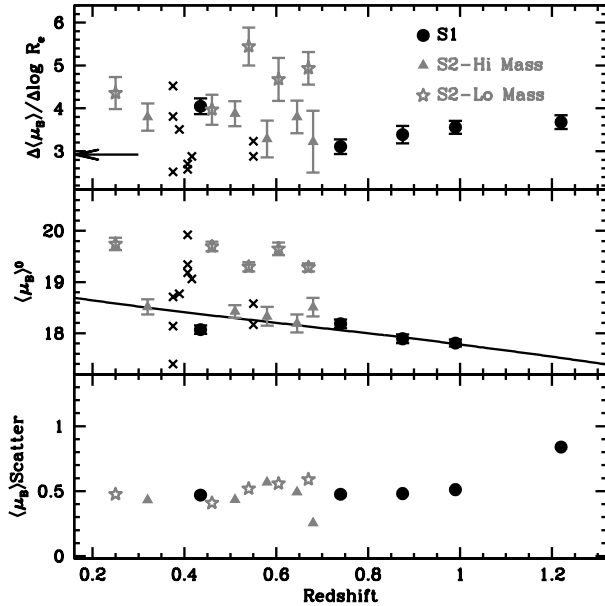


**Figure 11.** Redshift evolution of the Kormendy relation. Sample S1 is shown as black circles, sample S2 (grey) has been split with respect to the median stellar mass within that sample ( $3.5 \cdot 10^{10} M_{\odot}$ ). The bins in redshift are chosen such that the number of galaxies per bin is constant for each set. A Kormendy relation is fit, and this plot gives the slope (*top*), zero point (*middle*; in  $\text{mag arcsec}^{-2}$ ) and biweight scatter about the best fit (*bottom*; in  $\text{mag arcsec}^{-2}$ ). The arrow in the top panel is the  $z=0$  slope obtained by La Barbera et al. (2003) and the crosses are the cluster observations of Ziegler et al. (1999). The line in the middle panel corresponds to the evolution of an exponentially decaying star formation rate started at  $z_F=5$ , with timescale  $\tau = 0.5$  Gyr and solar metallicity.

combination of younger stellar populations and a significantly different surface brightness profile compared to more massive early-type galaxies, similar to the  $z = 0$  case (Graham & Guzmán 2003).

## 6 SUMMARY AND CONCLUSIONS

We present a sample of visually-classified early-type galaxies over the  $360 \text{ arcmin}^2$  area covered by the ACS/*HST* images of the Great Observatories Origins Deep Survey (GOODS, Giavalisco et al. 2004), including both the North and South fields. The classification is only limited in flux ( $i_{AB} < 24$ ), i.e. no colour cuts or surface brightness profile constraints are imposed in the selection. The sample comprises 910 early-type galaxies, for which we compile spectroscopic quality redshifts from publicly available datasets for 541 galaxies (i.e.  $\sim 60\%$  of the total sample). For the rest we estimate photometric redshifts from available data (both *HST* and ground-based). We find the comoving number density to depend strongly on stellar mass, such that the number of galaxies with  $M_s \gtrsim 10^{11} M_{\odot}$  only increases a factor 2 between  $z=1$  and  $z=0$ , whereas the number of galaxies with stellar mass  $10^{10} < M_s/M_{\odot} < 10^{11}$  increase a factor  $\sim 50$  in the same redshift range. In the full, flux-limited sample, we find 26% of our early-types are blue (i.e. corresponding to a star formation history with timescale longer than 1 Gyr, or with a significant amount of young stars). This fraction is similar to the number of low-redshift early-types with a significant amount of recent star formation (Kaviraj et al. 2007).

The depth and superb resolution of the ACS images enable us

to explore the *intrinsic* colour distribution. We perform a technique based on a Voronoi tessellation (already applied in Ferreras et al. 2005) that allows a robust determination of the radial colour gradient and scatter. In figure 6 we show that the colour gradients are strongly dependent on the overall photometric type, such that red galaxies have mostly red cores and blue early-type galaxies have blue cores. This is a non-trivial statement, as one could imagine star formation in the outer parts of the galaxy, resulting in blue galaxies with red cores. We find central star formation in otherwise red galaxies is very rare. On the other hand, the majority of galaxies with (recent) star formation exhibit most of this star formation in their centers. These observations suggest an inside-out formation process in these galaxies, ruling out recent attempts at explaining elliptical galaxy formation with an outside-in formation scenario (Pipino et al. 2006). An inside-out scenario implies that regardless of the way star formation is triggered – primordial collapse versus merging/interactions, gas is accumulated towards the centre, starting star formation in the central regions, subsequently “diffusing” outwards. One could argue whether the mechanism explaining these blue cores reduces to minor mergers (Ellis et al. 2001; Kaviraj et al. 2007b). Robust confirmation of the actual cause of these blue cores will require the analysis of abundance ratio gradients (see e.g. Ferreras & Silk 2002).

Figure 8 shows that the local observations of radial colour gradients in elliptical galaxies (e.g. Peletier 1990) mostly correspond to a range of metallicities. This can be thought of as the *intrinsic* equivalent of the pure metallicity sequence of Kodama & Arimoto (1997), used in that paper to explain the colour-magnitude relation *among* galaxies. Our results are in agreement with the sample of cluster galaxies at low and moderate redshift (Tamura & Ohta 2000; La Barbera et al. 2004), but our sample increases by an order of magnitude the number and accuracy of the colour gradient estimates. La Barbera et al. (2004) only find optical colour gradients compatible with zero slope. We do find non-zero, albeit small, optical gradients and a significant trend with stellar mass, such that the most massive galaxies have almost always red cores.

Defining volume-limited samples, we find that blue galaxies only contribute 4% to the total number of bright ( $M_V < -21$ ) early-type galaxies out to  $z < 1.4$ . Most of the blue early-type galaxies in our – visually classified – sample correspond to low-mass systems, and are removed when taking volume-limited samples. At face value, we could state that significant star formation in early-type galaxies only takes place for galaxies less massive than  $M_s \sim 10^{10} M_{\odot}$  even out to redshifts  $z \sim 1$ . As shown by Bell et al. (2007), star formation in a substantial fraction of blue cloud galaxies needs to be shut off between  $z=1$  and  $z=0$ , making them evolve to the red sequence, thereby explaining the significant growth in mass there. However, in addition to considering the contribution with respect to mass and star formation history, it is also well known that blue cloud and red sequence differ morphologically, with spiral and irregular galaxies dominating the blue cloud whereas red sequence galaxies are mostly early-types. Since our sample of early-types was selected on pure morphological grounds, those early-types with (recent) star formation confirm the scenario of Bell et al. (2007), in that these objects will not only evolve onto the red sequence in terms of colour, but also in terms of morphology.

The Kormendy relation was explored in two volume-limited samples and a remarkable consistency is found with the KR at  $z=0$ , with no significant change of the slope of the Kormendy relation out to  $z \sim 1.2$ . The scatter about the best fit does not change significantly either. Only the average surface brightness is found to change in the

Kormendy relation, with an evolution consistent with pure passive evolution of old stellar populations.

## ACKNOWLEDGMENTS

We thank Bahram Mobasher for useful comments about the paper, and Alister Graham for providing us with his code to compute correction factors for magnitudes and radii. IF acknowledges the Nuffield foundation for partial support of this project. T.L. is supported within the framework of the Excellence Initiative by the German Research Foundation (DFG) through the Heidelberg Graduate School of Fundamental Physics (grant number GSC 129/1). This paper is based on observations made with the NASA ESA *Hubble Space Telescope*, obtained from the data archive at the Space Telescope Science Institute, which is operated by the Association of Universities for Research in Astronomy, Inc. under NASA contract NAS 5-26555. The NIR observations have been carried out using the Very Large Telescope at the ESO Paranal Observatory under Program ID:LP168.A-0485

## REFERENCES

- Abraham, R. G., Valdes, F., Yee, H. K. C. & van den Bergh, S. 1994, *ApJ*, 432, 75
- Beers, T. C., Flynn, K. & Gebhardt, K. 1990, *AJ*, 100, 32
- Bell, E., et al., 2007, *ApJ*, 663, 834
- Bershady, M. A., Jangren, A., & Conselice, C. J. 2000, *AJ*, 119, 2645
- Bertin, E. & Arnouts, S. 1996, *A&AS*, 117, 393
- Bower R. G., Lucey J. R., Ellis R., 1992, *MNRAS*, 254, 589
- Bruzual, G. & Charlot, S., 2003, *MNRAS*, 344, 1000
- Capaccioli, M., Caon, N., D’Onofrio, M., 1992, *MNRAS*, 259, 323
- Capak, P. et al., 2004, *AJ*, 127, 180
- Cappellari, M., Copin, 2003, *MNRAS*, 342, 345
- Chabrier, G., 2003, *PASP*, 15, 763
- Cole, S., Lacey, C. G., Baugh, C. M., Frenk, C. S., 2000, *MNRAS*, 319, 168
- Conselice, C. J., et al. 2007, *MNRAS*, 381, 962
- Croton, D. J., et al. 2005, *MNRAS*, 356, 1155
- Djorgovski, S., Davis, M., 1987, *ApJ*, 313, 59
- De Lucia, G. Springel, V., White, S. D. M., Croton, D., Kauffmann, G., 2003, *MNRAS*, 343, 75
- di Serego Alighieri, S., et al., 2005, *A&A*, 442, 125
- Ellis, R. S., Smail, I., Dressler, A., Couch, W. J., Oemler, A. J., Butcher H., Sharples, R. M., 1997, *ApJ*, 483, 582
- Ellis, R. S., Abraham, R. G., Dickinson, M., 2001, *ApJ*, 551, 111
- Ferreras, I., Silk, J., 2000, *ApJ*, 541, L37
- Ferreras, I., Silk, J., 2002, *MNRAS*, 336, 1181
- Ferreras, I., Silk, J., 2003, *MNRAS*, 344, 455
- Ferreras, I., Lisker, T., Carollo, C. M., Lilly, S. J., & Mobasher, B. 2005, *ApJ*, 635, 243
- Ferreras, I., Saha, P. & Burles, S. 2008, *MNRAS*, 383, 857
- Ferreras, I., Lisker, T., Pasquali, A., Khochfar, S., Kaviraj, S. 2008, *MNRAS Letter*, submitted.
- Fitzpatrick, E. L., 1999 *PASP*, 111, 63
- Fontana, A. et al., 2006, *A&A*, 459, 745
- Forbes, D. A., Ponman, T. J., Brown, R. J. N., 1998, *ApJ*, 508, L43
- Graham, A. W. & Driver, S. P. 2005, *Publications of the Astronomical Society of Australia*, 22, 118
- Graham, A. W., Guzmán, R., 2003, *AJ*, 125, 2936
- Graham, A. W., Driver, S. P., Petrosian, V., Conselice, C. J., Bershady, M. A., Crawford, S. M., & Goto, T. 2005, *AJ*, 130, 1535
- Giavalisco, M. et al., 2004, *ApJ*, 600, L93
- Hatton, S., Devriendt, J. E. G., Ninin, S., Bouchet, F. R., Guiderdoni, B., Vibert, D., 2003, *MNRAS*, 343, 75
- Ilbert, O. et al., 2006, *A&A*, 453, 809
- Jørgensen, I., Franx, M. & Kjaergaard, P., 1995, *MNRAS*, 273, 1097
- Jørgensen, I., Franx, M., Kjaergaard, P., 1996, *MNRAS*, 280, 167
- Kaviraj, S., Devriendt, J. E. G., Ferreras, I., Yi, S. K., 2005, *MNRAS*, 360, 60
- Kaviraj, S., GALEX Science Team, 2007, *ApJS*, 173, 619
- Kaviraj, S., Peirani, S., Khochfar, S., Silk, J., Kay, S., 2007, arXiv:0711.1493
- Kaviraj, S., MUSYC collaboration, 2008, *MNRAS*, 388, 67
- Kaviraj, S., 2008, *MPLA*, 23, 153
- Khochfar, S., Silk, J. 2006, *ApJ*, 648, L21
- Kodama, T., Arimoto, N., 1997, *A&A*, 320, 41
- Kormendy, J., 1977, *ApJ*, 218, 333
- Krist, J., 1993, *ASP Conf. Ser. 52: Astronomical Data Analysis Software and Systems II*, 2, 536
- La Barbera, F., Busarello, G., Massarotti, M., Merluzzi, P., Capaccioli, M., 2003, *ApJ*, 595, 127
- La Barbera, F., Merluzzi, P., Busarello, G., Massarotti, M., Mercurio, A., 2004, *A&A*, 425, 797
- Lisker, T., Grebel, E. K., Binggeli, B., & Glatt, K. 2007, *ApJ*, 660, 1186
- Lotz, J. M., Primack, J., & Madau, P. 2004, *AJ*, 128, 163
- Menanteau, F., Abraham, R. G., Ellis, R. S., 2001, *MNRAS*, 322, 1
- Menanteau, F., et al., 2004, *ApJ*, 612, 202
- Menanteau, F., et al., 2005, *ApJ*, 620, 697
- Mobasher, B., et al., 2004, *ApJ*, 600, L167
- Mobasher, B., et al., 2007, *ApJS*, 172, 117
- Pasquali, A., et al., 2006, *ApJ*, 636, 115
- Petrosian, V. 1976, *ApJ*, 209, L1
- Peletier, R. F., Davies, R. L., Illingworth, G. D., Davis, L. E., Cawson, M., 1990, *AJ*, 100, 1091
- Pipino, A., Matteucci, F., Chiappini, C., 2006, *ApJ*, 638, 739
- Popesso, et al., 2008, *A&A*, submitted, arXiv:0802.2930
- Saglia, R. P., Colless, M., Baggle, G., Bertschinger, E., Burstein, D., Davies, R. L., McMahan, R. K., Wegner, G., 1997, in Arnaboldi, M., Da Costa, G. S., Saha, P., eds, *ASP Conf. Ser. 116: The Nature of Elliptical Galaxies; 2nd Stromlo Symposium The EFAR Fundamental Plane*. pp 180–
- Scarlati, C., et al. 2007, *ApJS*, 172, 494
- Schade, et al. 1999, 525, 31
- Schlegel, D. J., Finkbeiner, D. P. & Davis, M., 1998, *ApJ*, 500, 525
- Sersic, J. L. 1968, Córdoba, Atlas de Galaxias Australes, Argentina: Observatorio Astronomico.
- Stanford, S. A., Eisenhardt, P. R. M., Dickinson, M., 1998, *ApJ*, 492, 461
- Tamura, N., Ohta, K., 2000, *AJ*, 120, 533
- Thomas, D., Greggio, L., Bender, R., 1999, *MNRAS*, 302, 537
- Treu, T., Stiavelli, M., Casertano, S., Møller, P., Bertin, G., 2002, *ApJ*, 564, L13
- Trujillo, I., Conselice, C. J., Bundy, K., Cooper, M. C., Eisenhardt, P. & Ellis, R. S. 2007, *MNRAS*, 382, 109

- van Dokkum, P. G., Franx, M., 1996, MNRAS, 281, 985  
van Dokkum, P. G., Franx, M., Fabricant, D., Illingworth, G. D.,  
Kelson, D. D., 2000, ApJ, 541, 95  
Van Dokkum, P. et al., 2008, ApJ, 677, L5  
Vanzella, E. et al., 2008, A&A, 478, 83  
Wirth, G., et al., 2004, AJ, 127, 3121  
Ziegler, B. L., Saglia, R. P., Bender, R., Belloni, P., 1999, A& A,  
346, 13

## APPENDIX A: EXTRACTION OF SIZES AND MAGNITUDES FROM THE ACS IMAGES

As discussed in §2.1 it is important to correct for the loss of light expected for a typical surface brightness distribution. In order to estimate the accuracy of the retrieved size, apparent magnitude and surface brightness we ran a number of simulations, generating postage stamps with the same noise characteristics as the ones taken from the ACS images. The simulations correspond to smooth distributions of galaxies with a Sersic profile (Sersic 1968). The simulations realistically map the error in each pixel using the weight maps of the ACS images to determine a correlation between surface brightness per pixel and S/N.

For a given choice of apparent magnitude and half-light radius we generate  $501 \times 501$  stamps with the same pixel size as the ACS images (0.03 arcsec). For each galaxy in the ensemble we take a random value for the Sersic index (between  $n = 2$  and 4); ellipticity (between  $e = 0$  and 0.6) and position angle. A total of 16 ensembles are generated for four different values of apparent magnitude ( $i_{F775W} = \{18, 20, 22, 24\}$ ) and half-light radius ( $R_e = \{5, 8, 10, 20\}$  pixels). Each model galaxy is convolved by the PSF of ACS in the  $i$  band (obtained from a set of stellar images as discussed in §4) and is passed through the same code as the original sample to determine the half-light radius, magnitude and surface brightness.

Figure A1 shows the result ( $1\sigma$  error bars). Notice the systematic trend in the offset with respect to half-light radius (*left*) or concentration (measured as  $R_{90}/R_{50}$ ; *right*). The figure also shows that the correction should depend to first order on  $R_e$ , whereas concentration is a second-order correction. The total sample of 8,000 galaxies is split about the median value of  $R_{90}/R_{50}$ , showing the most concentrated galaxies in black. Our results are consistent with Graham et al. (2005), as concentration correlates with Sersic index. However our regime of observations is different from their work, as our galaxies have sizes significantly closer to the PSF.

The simulations shown in figure A1 motivate a simple correction dominated by  $R_e$  with concentration modelled as a linear change to the zero point of the correction. The corrections – shown in the leftmost panels of figure A1 for the median value of  $R_{90}/R_{50}$  – are:

$$R_{\text{out}} = R_{\text{in}} \left( 0.57 + 1.5e^{-0.2R_{\text{in}}} - 0.244 \frac{R_{90}}{R_{50}} \right), \quad (\text{A1})$$

and

$$i_{\text{out}} = i_{\text{in}} + 0.05 + 0.003R_{\text{in}} + 0.068 \frac{R_{90}}{R_{50}}, \quad (\text{A2})$$

with the radii given in pixels. These two expressions are used to make a correction on apparent magnitude and half-light radius. In order to assess the accuracy after the corrections we generate four samples of 910 simulated galaxies with the same apparent magnitude and size as our observed sample. The Sersic index, ellipticity and position angle are chosen randomly in the same way as described above. Figure A2 shows the histograms comparing recovered and original size, magnitude and apparent surface brightness after applying the corrections given by equations A1 and A2. The lines are Gaussian fits to the data, with the standard deviation shown in the top left corner of each panel. These are our *official* uncertainties, namely 9% in  $R_e$ , 0.05 mag in the *TOTAL*  $i_{F775W}$  magnitude and 0.16 mag/arcsec<sup>2</sup> in  $i_{F775W}$  apparent surface brightness.

## APPENDIX B: RECOVERING STELLAR MASSES

The stellar masses presented in this paper are extracted from the total apparent  $i_{F775W}$  magnitudes. One could argue that NIR photometry might be a more reliable tracer of the stellar mass. To confirm the validity of  $i_{F775W}$  photometry *over the redshift range probed by our sample*, we show in figure B1 the predicted mass for a  $i_{F775W} = 23$  (AB) galaxy (*top*) or a  $K_s = 22$  (AB) galaxy (*bottom*). The result is shown according to photometric type, with the left (right) panels showing red (blue) galaxies. The models are identical to those described in §2.3. The dark grey shading gives the expected stellar mass as a function of redshift, and – to guide the eye – we include a vertical line at  $z=0.7$  (roughly the median redshift of the sample). As expected, for a later (i.e. bluer) photometric type, the stellar mass is smaller. One should emphasize here that within our volume-limited subsamples S1 and S2, the fraction of galaxies corresponding to the panels on the right amount only to 4 and 11%, respectively.

The horizontal light grey shading shows a 0.3 dex uncertainty in stellar mass for a  $z=0.7$  galaxy. Notice that in this redshift range  $i_{F775W}$  is as accurate a tracer of stellar mass as  $K_s$ , notwithstanding the fact that the high resolution of the ACS images allows us to determine more accurately the *TOTAL* apparent magnitude of the galaxies.

As a second check, we retrieved the publicly available ISAAC/*VLT*  $K_s$  images of the GOODS/CDFS field (Retzlaff et al., in preparation). The images were analysed with SExtractor (Bertin & Arnouts 1996) using the provided zero point and weight maps. The catalogue of detected sources was cross-correlated with our sample, and only those galaxies with a SExtractor `flag=0` were selected for the comparison. We used MAG\_BEST and further applied the same correction to obtain total magnitudes as in appendix A. Figure B2 shows the comparison, along with the equivalent Gaussian distribution, which has a mean of  $\langle \log M_s(K_s) - \log M_s(i) \rangle = -0.04$  dex and standard deviation 0.13 dex. The mean and standard deviation are reduced to  $-0.02$  and 0.11 dex, respectively when the sample is restricted to  $i_{F775W} < 23$  galaxies. We conclude that our  $i$ -band extracted stellar masses are accurate to within the quoted 0.3 dex uncertainty (including population synthesis effects).

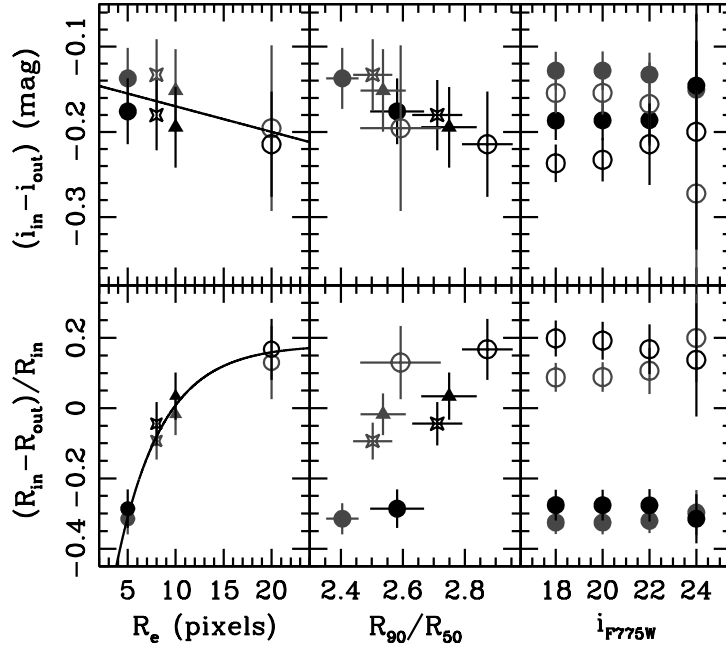


**Figure A1.** Recovered  $i_{F775W}$  (top), and half-light radius (bottom) of simulated galaxies,  $1\sigma$  error bars shown. Each symbol corresponds to a choice of  $R_e$ . The sample of 8,000 simulated galaxies is separated with respect to  $R_{90}/R_{50}$ , such that the grey (black) dots represent the subsample below (above) the median. The highest discrepancy in the recovery of the half-light radius occurs for values close to the FWHM of the PSF ( $\sim 3$  pixels). The simulations are shown with respect to  $R_e$  (left), concentration *middle* – measured as  $R_{90}/R_{50}$  – and apparent magnitude (*right*). The lines in the leftmost panels give the corrections used for flux and half-light radius (equations A1 and A2) at the median value of concentration. Notice that the panels on the right only show the subsamples with the largest and smallest value of  $R_e$  to avoid crowding the figure.

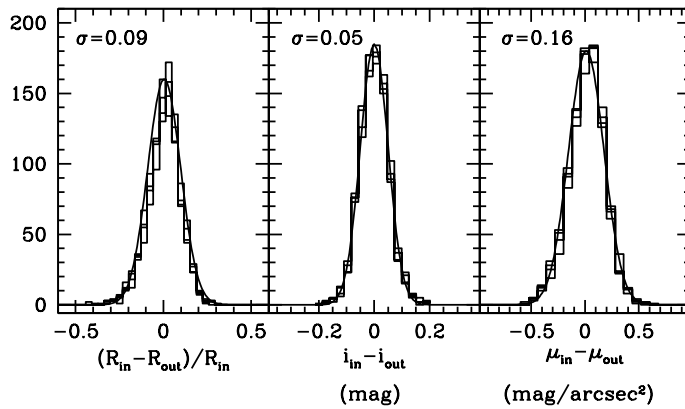


**Figure A2.** Recovery of four simulated samples of 910 galaxies with the same distribution in apparent magnitude and size as the original sample. The histograms compare the original and the recovered size (*left*); magnitude (*middle*) and apparent surface brightness along with a Gaussian that characterizes the uncertainty for the complete sample.

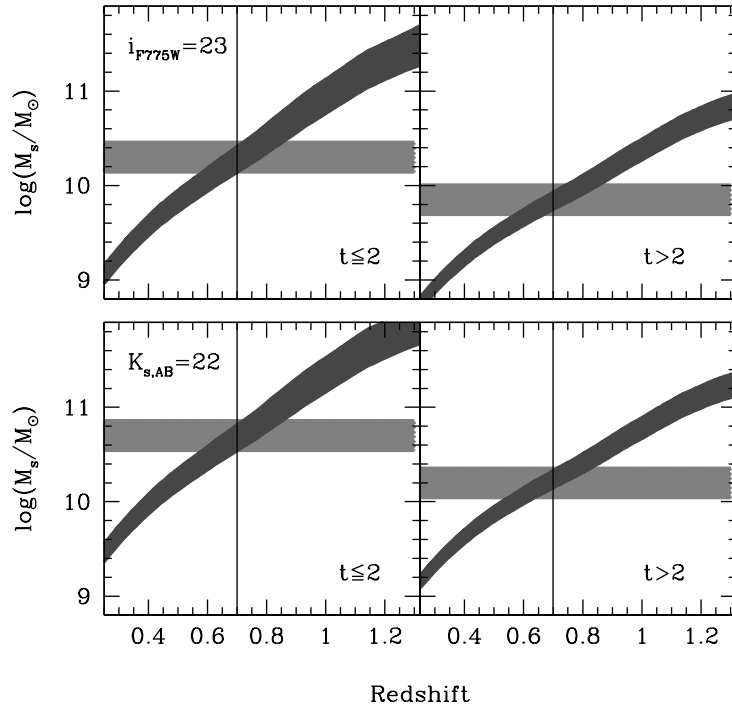


**Figure B1.** Comparing the accuracy of stellar mass estimates using  $i_{F775W}$  (*top*) vs a more “traditional” method with NIR magnitudes (*bottom*). A fiducial apparent magnitude is assumed as labelled. The dark grey region gives the stellar mass expected as a function of redshift for photometrically “red” (*left*) and “blue” galaxies. To guide the eye, we assume a  $z=0.7$  galaxy (vertical line). The light gray horizontal shading represents a 0.3 dex uncertainty about the predicted value. Notice both  $i_{F775W}$  and  $K_s$  give similar accuracy over the redshift probed by our sample.

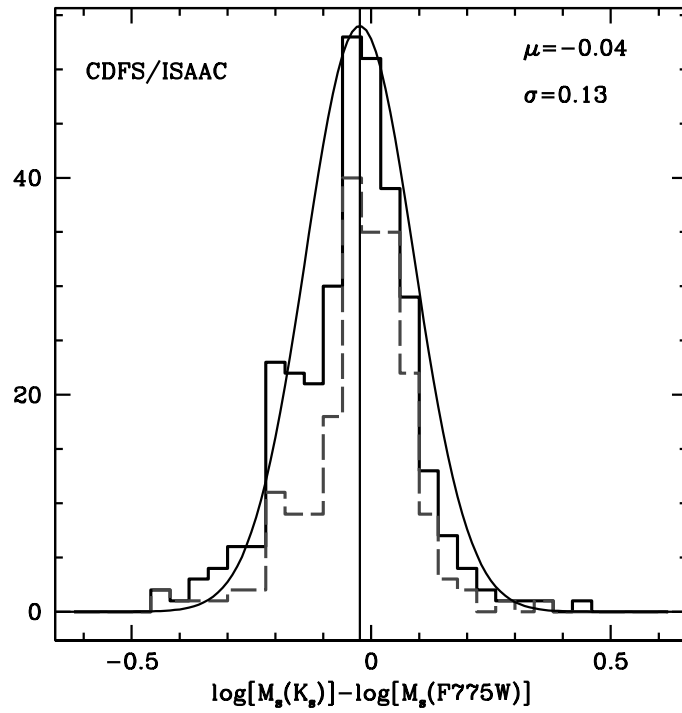


**Figure B2.** Comparison between stellar masses from this work – extracted from the *corrected* F775W magnitudes – and NIR masses using the  $K_s$  magnitudes of the CDFS using the ISAAC images (Retzlaff et al., in preparation). Identical flux corrections are applied to the NIR magnitudes as those obtained for F775W (see appendix A). The grey histogram corresponds to a subsample of the brighter ( $i_{F775W} < 23$ ) galaxies, which give an offset of  $\mu = -0.02$  and a standard deviation of  $\sigma = 0.11$  dex.